

Accepted by PASP on May 2, 2006

The Anisoplanatic Point Spread Function in Adaptive Optics

M. C. Britton

California Institute of Technology, Pasadena, CA 91125

`mbritton@astro.caltech.edu`

ABSTRACT

The effects of anisoplanatism on the adaptive optics point spread function are investigated. A model is derived that combines observations of the guide star with an analytic formulation of anisoplanatism to generate predictions for the adaptive optics point spread function at arbitrary locations within the field of view. The analytic formulation captures the dependencies of anisoplanatism on aperture diameter, observing wavelength, angular offset, zenith angle and turbulence profile. The predictions of this model are compared to narrowband $2.12\text{ }\mu\text{m}$ and $1.65\text{ }\mu\text{m}$ images of a 21 arcsec binary ($m_v=7.3, 7.6$) acquired with the Palomar Adaptive Optics System on the Hale 5 meter telescope. Contemporaneous measurements of the turbulence profile made with a DIMM/MASS unit are used together with images of the primary to predict the point spread function of the binary companion. Predicted companion Strehl ratios are shown to match measurements to within a few percent, whereas predictions based on the isoplanatic angle approximation are highly discrepant. The predicted companion point spread functions are shown to agree with observations to 10%. These predictions are used to measure the differential photometry between binary members to an accuracy of 1 part in 10^3 , and the differential astrometry to an accuracy of 1 mas. Errors in the differential astrometry are shown to be dominated by differential atmospheric tilt jitter. These results are compared to other techniques that have been employed for photometry, astrometry, and high contrast imaging.

Subject headings: instrumentation:adaptive optics, techniques: high angular resolution, techniques: photometric

1. Introduction

An adaptive optics system senses phase aberrations arising from atmospheric turbulence using observations of a guide star, and compensates these aberrations by applying a correction to an adaptive mirror. This compensation is valid in the direction of the guide star, but degrades with

angular offset from the guide star due to anisoplanatism. This effect arises due to the shearing between the columns of turbulent atmosphere traversed by light from the guide star and light from a target at a finite angular offset.

The phase aberrations that arise from anisoplanatism depend on a number of parameters. The errors grows with angular offset from the reference source, so that image quality and Strehl ratio degrade with increasing angular offset. The vertical distribution of turbulence has a strong effect on the degree of error, with higher altitude turbulence generating larger errors due to the larger geometrical shear. This dependence varies in time as the distribution of atmospheric turbulence over the telescope evolves. The anisoplanatic error grows with zenith angle, since one sees more turbulence along line of sight to the object. The error is also a strong function of aperture diameter and observing wavelength.

This large number of dependencies yields a rich phenomenology for the adaptive optics point spread function (PSF). The parameter space is so large that it is not practical to integrate long enough to attain the stochastically averaged PSF. The variability in the adaptive optics PSF is a serious impediment to the quantitative interpretation of observations, and can limit the precision in astronomical applications involving photometry, astrometry, crowded field imaging, and high dynamic range imaging of extended objects. Integral field unit spectroscopy of extended objects is another application in which the dynamic range of observations may be seriously compromised by PSF variability.

Multiconjugate (Beckers 1988) and multiobject (Hammer et al. 2004; Ellerbroek et al. 2005) adaptive optics architectures have been proposed that aim to directly overcome the effects of anisoplanatism. These architectures use multiple guide stars distributed over a finite field of view and employ tomographic algorithms to estimate the three dimensional volume of atmospheric turbulence. The algorithms rely on a knowledge of the angular offsets among the guide stars, and use the statistical correlations induced by these angular offsets in order to effect the turbulence estimation. In this sense, these algorithms employ anisoplanatism in order to overcome the effects of anisoplanatism. Anisoplanatism in a single conjugate adaptive optics system forms the limiting case of this more complex problem. On-sky tests with existing adaptive optics systems can serve an important role in validating our understanding of anisoplanatism and increasing our confidence in the success of tomography.

Significant efforts have been directed towards overcoming the effects of anisoplanatism in existing adaptive optics systems. One line of investigation has aimed to extract estimates of the PSF from observed data. For a small target field, the PSF may be assumed to be field independent. Observations of such fields that contain multiple point sources may be deconvolved using a reference PSF selected from the data or by solving for the optimal PSF during deconvolution. These approaches have been applied to crowded stellar fields (Diolaiti et al. 2000; Christou et al. 2004) and planetary objects (de Pater et al. 2004). In an effort to calibrate wider fields, Steinbring et al. (2002) measured the effects of anisoplanatism on the PSF using observations of crowded fields,

and then applied these measurements to other fields of interest. This type of technique is unable to capture any temporal evolution of the turbulence profile that occurs between the observations. Another approach has employed a parameterized model of the effects of anisoplanatism on the adaptive optics PSF, extracting these parameters during the deconvolution procedure (Flicker & Rigaut 2005).

The above techniques did not attempt to use any independent information about the turbulence profile in estimating the adaptive optics PSF. Other researchers have incorporated such measurements into the PSF estimates. Voitsekhovich et al. (1998) computed the structure function due to residual phase aberrations from anisoplanatism, and used this to evaluate the Strehl ratio as a function of angular offset from the guide star for different turbulence profiles and aperture diameters. Fusco et al. (2000) derived an expression for the adaptive optics optical transfer function that captured the dependencies of anisoplanatism on the above parameters. These authors carried out 850 nm observations of two binaries with the ONERA adaptive optics system and used a turbulence profile measured from a balloon flight together with the analytical expression for the OTF to predict the binary companion PSF. Weiß et al. (2002) performed K band adaptive optics observations of a binary using the ALFA adaptive optics system while at the same time measuring the turbulence profile using a scidar instrument. These authors compared the Strehl ratio degradation due to anisoplanatism measured from the binary image data with that expected from the measured turbulence profiles. These experiments have shown a promising level of agreement between predictions and measurements.

Recent work in the area of turbulence monitoring has yielded an automated set of equipment capable of delivering real time estimates of the turbulence profile on minute timescales (Tokovinin et al. 2005). This equipment is based on the combination of a Multi-Aperture Scintillation Sensor (MASS) (Kornilov et al. 2003) and a Differential Image Motion Monitor (DIMM) (Vernin & Munoz-Tunon 1995). This turbulence monitoring equipment is now being used at a number of different sites, and has been employed by the Thirty Meter Telescope project for its site testing program (Skidmore et al. 2004). As part of this program, a set of this equipment has been installed at Palomar Observatory.

This paper describes an experiment in which measurements of the turbulence profile from the DIMM/MASS equipment and short exposure images of a 21 arcsec binary from the Palomar Adaptive Optics System on the Hale 5 meter telescope were acquired contemporaneously over the course of several hours. Section 2 presents the analysis of anisoplanatism used for this experiment. Section 3 describes the observations, while Section 4 and 5 describe the analysis and results of the experiment.

2. A Model for the Field Dependent AO PSF

2.1. Model Formulation

Consider an adaptive optics system that measures the wavefront phase aberrations $\phi_a(\vec{r})$ in the direction of a guide star and compensates these aberrations using an adaptive mirror. Here \vec{r} is a vector in the pupil plane of the telescope. An adaptive optics system is not capable of effecting a perfect correction, and residual phase aberrations $\tilde{\phi}_a(\vec{r})$ will be present in the guide star wavefront after adaptive compensation. The wavefront phase aberrations $\phi_b(\vec{r})$ in another direction on the sky differ from those of the guide star due to anisoplanatism. In this direction, the residual aberrations that remain after compensation by the adaptive optics system are

$$\Delta\phi(\vec{r}) = \phi_b(\vec{r}) - \phi_a(\vec{r}) + \tilde{\phi}_a(\vec{r}) \quad (1)$$

This simple model does not account for time delay in the application of the adaptive correction. During this delay the wind carries turbulence past the telescope aperture, causing a servo error in the guide star wavefront. This turbulence evolution also induces correlations between the adaptive correction and the wavefront aberrations in other directions on the sky (Tyler 1983). Under certain observing conditions, this effect can lead to a situation where the Strehl ratio can be higher downwind of the guide star (Léna & Lai 1999). In this analysis, this wind induced anisoplanatic effect is neglected.

The structure function for a random process $\psi(\vec{r})$ is

$$D_\psi(\vec{r}_1, \vec{r}_2) = \langle \{\psi(\vec{r}_1) - \psi(\vec{r}_2)\}^2 \rangle \quad (2)$$

Using Equation 1, one can write the structure function for the residual phase $\Delta\phi(\vec{r})$ as

$$\begin{aligned} D_{\Delta\phi}(\vec{r}_1, \vec{r}_2) &= D_{\text{apl}}(\vec{r}_1, \vec{r}_2) + D_{\tilde{\phi}_a}(\vec{r}_1, \vec{r}_2) + \\ &2 \left\langle \left\{ \phi_{\text{apl}}(\vec{r}_1) \tilde{\phi}_a(\vec{r}_1) + \phi_{\text{apl}}(\vec{r}_2) \tilde{\phi}_a(\vec{r}_2) - \phi_{\text{apl}}(\vec{r}_1) \tilde{\phi}_a(\vec{r}_2) - \phi_{\text{apl}}(\vec{r}_2) \tilde{\phi}_a(\vec{r}_1) \right\} \right\rangle \end{aligned} \quad (3)$$

where $\phi_{\text{apl}}(\vec{r}) = \phi_b(\vec{r}) - \phi_a(\vec{r})$ is the component of the residual phase arising from anisoplanatism. The four cross terms in Equation 3 represent statistical correlations between the residual phase errors from the adaptive optics correction and those from anisoplanatism. A number of error terms that arise in adaptive optics systems have no correlation with anisoplanatic errors. Examples include measurement errors, aberrations in the optical system, and non-common path errors. In contrast, residual fitting error and servo error are weakly correlated with anisoplanatic errors. While the relative importance of these cross terms will depend on the error budget of the AO system, in many circumstances these terms will be small relative to the structure functions in Equation 3. Here, these cross terms are neglected.

With this approximation, the optical transfer function may be written as (Goodman 1985)

$$OTF(\vec{r}) = \int d\vec{s} \exp \left\{ -\frac{1}{2} \left[D_{\text{apl}}(\vec{s}, \vec{r} + \vec{s}) + D_{\tilde{\phi}_a}(\vec{s}, \vec{r} + \vec{s}) \right] \right\} W(\vec{s}) W(\vec{r} + \vec{s}) \quad (4)$$

where $W(\vec{r})$ is the pupil function. An issue of particular importance in evaluating the OTF is whether the structure functions of the two random processes are stationary over the pupil plane. For such a process, $D_\psi(\vec{r}_1, \vec{r}_2) = D_\psi(\vec{r}_2 - \vec{r}_1)$. As will be shown in the next section, $D_{\text{apl}}(\vec{r}_1, \vec{r}_2)$ is in fact stationary. This permits the OTF to be written as

$$\text{OTF}(\vec{r}) = \exp\left\{-\frac{1}{2}D_{\text{apl}}(\vec{r})\right\} \int d\vec{s} \exp\left\{-\frac{1}{2}D_{\tilde{\phi}_a}(\vec{s}, \vec{r} + \vec{s})\right\} W(\vec{s})W(\vec{r} + \vec{s}) \quad (5)$$

Note that the OTF has factored into a term that describes the anisoplanatic errors and a term that describes the residual errors in the direction of the guide star.

A relationship similar to Equation 5 was derived by Fusco et al. (2000), and represents a very important result. One may formulate the OTF in any direction on the sky from the product of the guide star OTF and an anisoplanatic transfer function formed from $D_{\text{apl}}(\vec{r})$. This factorization is of considerable use in the formulation of a practical scheme for evaluating the OTF, as discussed below.

2.2. The Anisoplanatic Structure Function

Prediction of the OTF in Equation 5 requires an evaluation of the anisoplanatic structure function $D_{\text{apl}}(\vec{r})$. This function may be computed using a semianalytic expression for the piston removed phase covariance on a circular aperture in the presence of Komolgorov turbulence (Tyler 1994). The covariance between the piston removed wavefront phase from two different sources at two different points \vec{r}_1 and \vec{r}_2 in the telescope pupil plane is given by

$$\langle \phi_a(\vec{r}_1) \phi_b(\vec{r}_2) \rangle = \Xi k^2 D^{5/3} \int_0^\infty dz C_n^2(z) \left[G_1 \left(\left| \frac{2}{D} \vec{r}_1 + \vec{\Omega}_{ab}(z) \right| \right) + G_1 \left(\left| \frac{2}{D} \vec{r}_2 - \vec{\Omega}_{ab}(z) \right| \right) - \left| \frac{2}{D} (\vec{r}_1 - \vec{r}_2) + \vec{\Omega}_{ab}(z) \right|^{5/3} - G_2 \left(\left| \vec{\Omega}_{ab}(z) \right| \right) \right] \quad (6)$$

Here D is the aperture diameter, k is the wavenumber, and $C_n^2(z)$ is the turbulence profile along the line of sight to the star. The numerical constant Ξ is given by

$$\Xi = \frac{1}{5} \left(\frac{1}{2} \right)^{7/3} \left[\Gamma \left(\frac{1}{6} \right) \right]^2 \left[\Gamma \left(\frac{1}{3} \right) \right]^{-1} = .458986 \quad (7)$$

where $\Gamma(z)$ is the Gamma function. The quantity $\vec{\Omega}_{ab}(z)$ is

$$\vec{\Omega}_{ab}(z) = \left(\frac{2z}{D} \right) \vec{\theta}_{ab} \quad (8)$$

where $\vec{\theta}_{ab}$ is the angular offset between the two sources. This parameter may be interpreted as the altitude dependent shear between the two beams. Finally, the two functions G_1 and G_2 in Equation

6 are defined in terms of the Gauss hypergeometric function

$${}_2F_1(a, b; c; x) = \sum_{n=0}^{\infty} \frac{\Gamma(a+n)\Gamma(b+n)\Gamma(c)}{\Gamma(a)\Gamma(b)\Gamma(c+n)} \frac{x^n}{n!} \quad (9)$$

as

$$G_1(x) = \begin{cases} \frac{6}{11} {}_2F_1\left(-\frac{11}{6}, -\frac{5}{6}; 1; x^2\right) & x \leq 1 \\ x^{5/3} {}_2F_1\left(-\frac{5}{6}, -\frac{5}{6}; 2; x^{-2}\right) & x \geq 1 \end{cases} \quad (10)$$

$$G_2(x) = \frac{8}{\pi} \int_0^1 dy \left[\cos^{-1} y - y\sqrt{1-y^2} \right] \begin{cases} (2y)^{8/3} {}_2F_1\left(-\frac{5}{6}, -\frac{5}{6}; 1; \left(\frac{x}{2y}\right)^2\right) & x \leq y \\ 2yx^{5/3} {}_2F_1\left(-\frac{5}{6}, -\frac{5}{6}; 2; \left(\frac{2y}{x}\right)^2\right) & x \geq y \end{cases} \quad (11)$$

Note that the covariance expression contains dependencies on observing wavelength, aperture diameter, turbulence profile, and angular offset between the two stars. The range variable z implicitly incorporates the dependence of the covariance on zenith angle, which enters through $C_n^2(z)$, $\vec{\Omega}_{ab}(z)$, and the range integral itself.

The expression for the covariance in Equation 6 is of great utility, and a number of familiar results in adaptive optics may be derived from this expression. Three limiting cases are shown in Appendix A: the phase structure function in the presence of uncompensated turbulence, the aperture averaged phase variance in the presence of uncompensated turbulence, and the aperture averaged residual phase variance due to anisoplanatism. These cases motivate the definition of the Fried parameter r_0 and the isoplanatic angle θ_0 , which are restated in this Appendix.

Expanding the expression for the anisoplanatic structure function using Equation 2 permits expression of $D_{\text{apl}}(\vec{r}_1, \vec{r}_2)$ as a sum over ten phase covariance terms involving $\phi_a(\vec{r})$ and $\phi_b(\vec{r})$. Direct evaluation of the resulting expression using Equation 6 yields

$$D_{\text{apl}}(\vec{r}_1, \vec{r}_2) = 2\Xi k^2 D^{5/3} \int_0^\infty dz C_n^2(z) \left\{ 2 \left| \vec{\Omega}_{ab} \right|^{5/3} + 2 \left| \frac{2}{D} (\vec{r}_1 - \vec{r}_2) \right|^{5/3} - \left| \frac{2}{D} (\vec{r}_1 - \vec{r}_2) + \vec{\Omega}_{ab} \right|^{5/3} - \left| \frac{2}{D} (\vec{r}_1 - \vec{r}_2) - \vec{\Omega}_{ab} \right|^{5/3} \right\} \quad (12)$$

This result indicates that the anisoplanatic structure function $D_{\text{apl}}(\vec{r}_1, \vec{r}_2)$ is in fact only a function of $\vec{r}_1 - \vec{r}_2$, and is therefore stationary over the pupil plane. This property permits the factorization of the anisoplanatic and guide star OTFs shown in Equation 5.

As in the case of the covariance, $D_{\text{apl}}(\vec{r})$ depends on observing wavelength, aperture diameter, turbulence profile, zenith angle and angular offset between the guide star and the direction of interest. Examples of the anisoplanatic structure function are shown in Figure 1 for a particular set of these parameters.

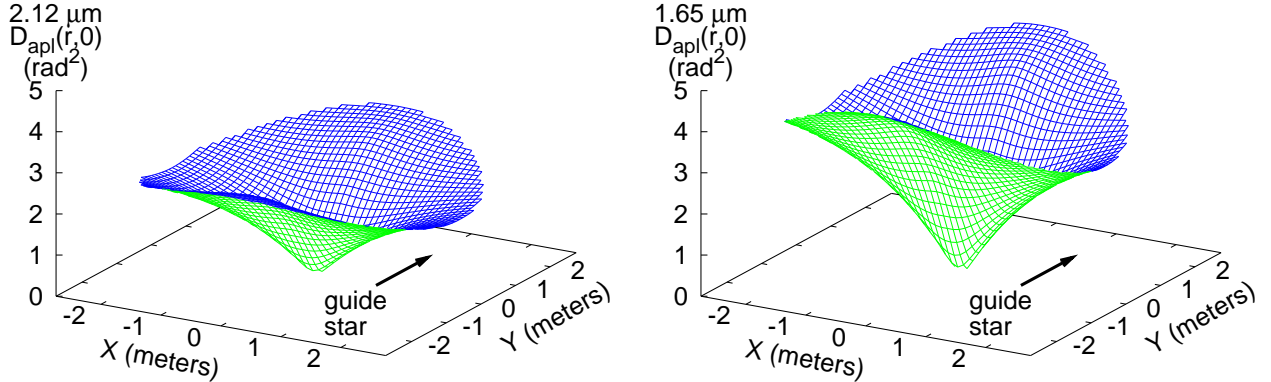


Fig. 1.— Anisoplanatic structure functions for a star at a 20 arcsec offset from the guide star, computed using Equation 12. The left and right panels show $D_{\text{apl}}(\vec{r}, 0)$ at observing wavelengths of $2.12 \mu\text{m}$ and $1.65 \mu\text{m}$ as a function of location \vec{r} within the pupil plane of a 5 meter telescope. The angular offset from the guide star was oriented along the Y axis, and the broken X-Y symmetry gives rise to the anisotropy apparent in these functions. This anisotropy is responsible for the radial elongation of the off axis PSF that is a characteristic feature of anisoplanatism. Despite this anisotropy the structure function is stationary over the pupil plane, so that $D_{\text{apl}}(\vec{r}_1, \vec{r}_2) = D_{\text{apl}}(\vec{r}_2 - \vec{r}_1)$. Typical atmospheric turbulence conditions at Palomar were assumed in these calculations.

2.3. The Anisoplanatic OTF and PSF

Equation 5 represents a model for the OTF at any point in the field of view. This quantity is a strong function of many parameters, which enter through both the anisoplanatic structure function $D_{\text{apl}}(\vec{r})$ and the guide star OTF. These dependencies give rise to the rich morphology in the adaptive optics PSF that presents such a challenge in the analysis of adaptive optics observations.

The classic dependence displayed by the adaptive optics PSF is its degradation with increasing angular offset from the guide star. Figure 2 contains a series of plots that illustrate this behavior for a 5 meter telescope under typical atmospheric turbulence conditions at Palomar. The first plot shows the aperture averaged residual RMS optical path difference (OPD) vs angular offset from the guide star. These results were computed by evaluating $\langle [\phi_{\text{apl}}(\vec{r})]^2 \rangle$ using Equation 6, and averaging this quantity over the pupil plane. The OPD is found by computing the square root of this result and dividing by k . Also shown in this plot is the OPD computed from the θ_0 approximation described in Appendix A. Even at small angular offsets, significant discrepancies exist between the exact result and the θ_0 approximation.

Consider an idealized adaptive optics system that acts to eliminate all wavefront error in the direction of the guide star, so that $\tilde{\phi}(\vec{r}) = 0$. In this case the OTF in Equation 5 depends only on the anisoplanatic structure function $D_{\text{apl}}(\vec{r})$, which may be evaluated using Equation 12. This allows computation of an OTF that incorporates only the effects of anisoplanatism, from which a

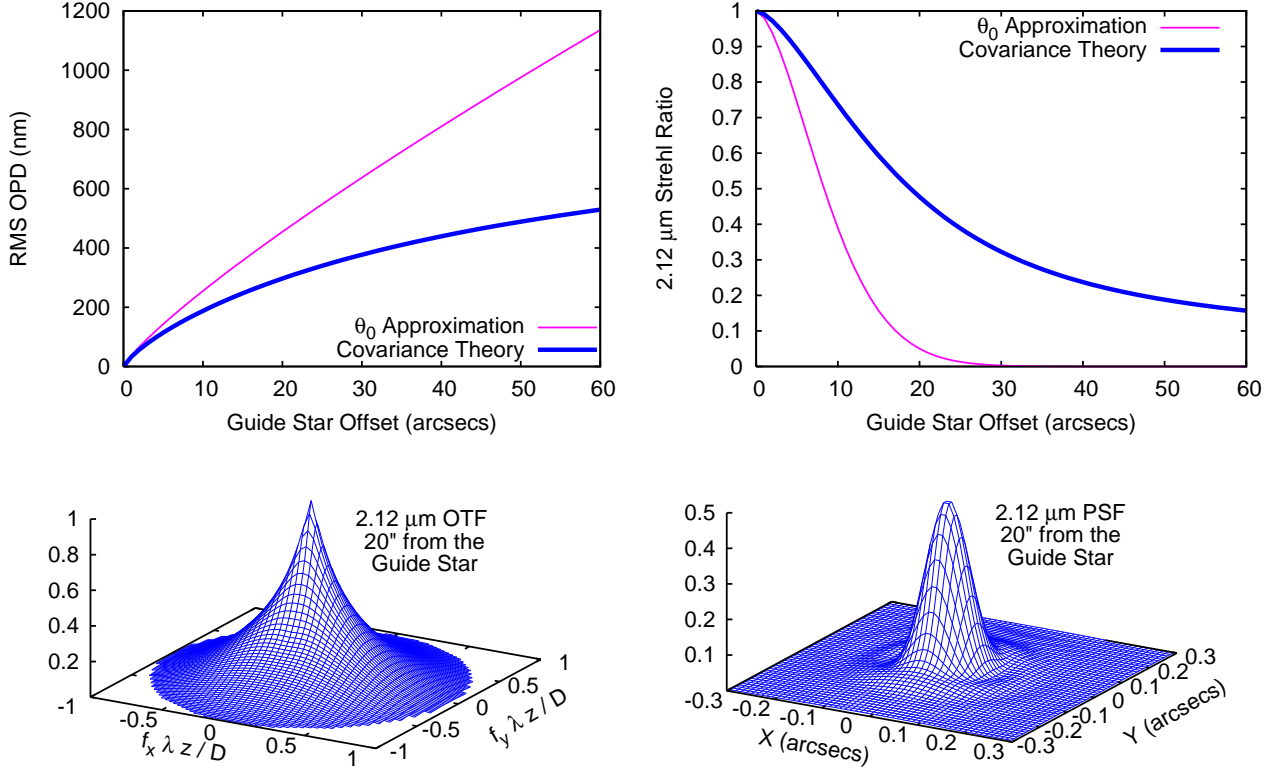


Fig. 2.— Illustrative effects of anisoplanatism on a 5 meter telescope, as described in the text. The upper left panel shows the aperture averaged residual RMS OPD due to anisoplanatism vs angular offset. The upper right panel shows the $2.12 \mu\text{m}$ Strehl ratio vs angular offset. The lower panels show the $2.12 \mu\text{m}$ anisoplanatic OTF and PSF at an angular offset of 20 arcsecs from the guide star. The PSF has been normalized by the peak value of the ideal, diffraction limited PSF. Typical atmospheric turbulence conditions for Palomar were assumed for these calculations.

PSF may be evaluated by Fourier transformation. Figure 2 shows the $2.12 \mu\text{m}$ anisoplanatic OTF and PSF at an angular offset of 20 arcsecs from the guide star, computed using this method. The PSF displays an increase in elongation along the direction to the guide star that is a characteristic of anisoplanatism. At this angular offset, the Strehl ratio has dropped to 47% due solely to the effects of anisoplanatism.

In the same way, the anisoplanatic Strehl ratio may be computed as a function of angular offset from the guide star. These results are also plotted in Figure 2. For comparison, the anisoplanatic Strehl ratios computed from the Marechal approximation are also shown. In this approximation, the aperture averaged phase variance computed from the θ_0 approximation was exponentiated to form an estimate of the anisoplanatic Strehl ratio. The combination of these two approximations significantly underestimates the anisoplanatic Strehl ratio computed directly from the anisoplanatic PSF.

This approach to evaluating the anisoplanatic OTF and PSF is illustrative, but the application of Equation 5 to observational data requires a treatment of the guide star OTF. While significant efforts have been made to estimate the guide star OTF using the statistical properties of $\tilde{\phi}_a(\vec{r})$ (Veran et al. 1997), evaluation of Equation 5 is considerably simplified if an observation of the guide star may be used in the prediction of the PSF elsewhere in the field of view. For this procedure to work, the guide star must itself be a point source. This is often the case in adaptive optics observations. In these circumstances, the guide star PSF may be extracted from the observational data and Fourier transformed to form the guide star OTF that appears in Equation 5. The anisoplanatic structure function $D_{\text{apl}}(\vec{r})$ may be evaluated from Equation 12 for the field point of interest. The only parameter in Equation 12 that is not defined by the observation is the turbulence profile, which may be measured using an independent set of equipment. The product of the observed guide star OTF and the anisoplanatic transfer function provides a prediction of the OTF at the field point of interest. Fourier transformation of this OTF yields a prediction for the PSF. There are no free parameters in this prediction.

3. Observations

To carry out a comparison of the model in Equation 5 with AO compensated image data, a set of observations was carried out at Palomar Observatory on the night of August 20, 2005. In this experiment, a well separated binary system was chosen and one member of the binary was used as the guide star for the Palomar Adaptive Optics system (Troy et al. 2000) on the Hale 5 meter telescope. A sequence of AO compensated near infrared images of the binary system from the PHARO infrared camera (Hayward et al. 2001) and a sequence of turbulence profiles from a set of DIMM/MASS equipment were acquired contemporaneously. Using the methodology presented in Section 2, a prediction for the PSF of the binary companion was formulated from the observed PSF of the guide star, the measured turbulence profiles, and the parameters defined by the observation. This prediction was then compared directly to the observed images of the binary companion. This section describes the details of these observations.

3.1. Turbulence Profile Measurements

Turbulence profile measurements were acquired using a DIMM/MASS unit on loan from the Thirty Meter Telescope Project. The unit itself has been described by Skidmore et al. (2004), and consists of a 35 cm robotic telescope that feeds both a DIMM and MASS instrument. The methodology employed in deriving turbulence profiles from the combination of DIMM and MASS measurements is discussed by Tokovinin et al. (2003) and references therein. The DIMM measures the differential motion between images acquired through two adjacent apertures. This measurement is sensitive to the integrated turbulence profile. A MASS unit measures the scintillation index of images acquired through four apertures of different radii. These measurements are sensitive to the

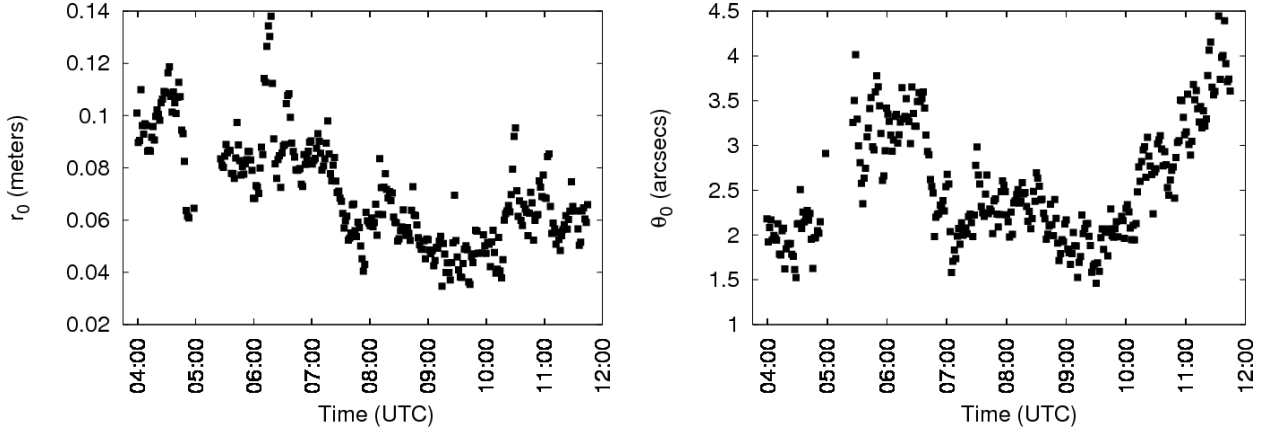


Fig. 3.— Turbulence parameters on the night of August 20, 2005 measured using the DIMM/MASS equipment at Palomar. These parameters were computed from the seven layer profiles estimated from the DIMM/MASS measurements, and are quoted at zenith and at a reference wavelength of $.5\text{ }\mu\text{m}$. The mean value of the Fried parameter r_0 was 7.1 cm, and that of the isoplanatic angle θ_0 was 2.54 arcsecs. Both parameters displayed considerable excursions from their means over the course of the night.

distribution of higher altitude atmospheric turbulence, which gives rise to scintillation. Together these measurements permit an estimate of the turbulence profile at altitudes of 0, .5, 1, 2, 4, 8 and 16 km. In a comparison of the turbulence strength measured at each of these layers, simultaneous MASS and scidar observations on Mauna Kea have displayed agreement to a factor of several (Tokovinin et al. 2005). One of the difficulties in the reconstruction of the turbulence profile from MASS data is that the procedure is somewhat ill-conditioned, in that simultaneously adjusting the layer altitude and the strength of turbulence can lead to similar scintillation indices. However, to leading order anisoplanatism displays this same type of covariance (*c.f.* Equation A13). In this sense both anisoplanatism and MASS are low resolution atmospheric profilometers.

The DIMM/MASS at Palomar Observatory was located 300 meters from the Hale 5m telescope. This unit was installed on the roof of a building approximately 10m above ground level. Turbulence profiles were measured about once every 90 seconds throughout the night of August 20th. For the first hour of the experiment, the DIMM/MASS unit tracked Beta Drac at $17^h30^m + 52^\circ18''$. A half hour gap in coverage occurred between 5:00 and 5:30 UT due to a tracking error experienced by the robotic telescope. From 5:30 UT onwards, the unit recorded images from Alpha Cep at $21^h19^m + 62^\circ35''$. For comparison, the binary imaged using the AO system was at $17^h59^m + 64^\circ08''$.

Figure 3 shows the values of r_0 and θ_0 computed from these profiles. Both of these parameters display deviations from their means of order a factor of two over the course of the night. The variability in the turbulence profiles imply a factor of two variation in the RMS OPD due to anisoplanatism. This in turn yielded pronounced variability in the Strehl ratio of the binary companion

that was readily detectable in the AO compensated image data.

3.2. Adaptive Optics Observations

Adaptive optics observations of the binary system HD164983 + HD164984 were acquired over a three hour period between 4:17 and 7:18 UT. This binary system has an angular separation of $21''$ and is oriented at 282° east of north. The Johnson V magnitudes of HD164983 and HD164984 are 7.6 and 7.3, respectively, and the latter source was used as the guide star for the adaptive optics system. The 25 arcsec field of view of the PHARO camera was used, permitting both binary members to be positioned on the detector simultaneously. Imaging was performed using two narrowband filters: an H2 filter with a central wavelength of $2.123\ \mu\text{m}$ and a bandpass of $.007\ \mu\text{m}$ and an FeII filter with a central wavelength of $1.648\ \mu\text{m}$ and a bandpass of $.03\ \mu\text{m}$. Exposure times of 2.8 seconds and 1.4 seconds were chosen for the H2 and FeII observations, respectively. The resulting stellar images peaked at less than 30% of the detector full well depth, which is well within the linear range of the detector. Images were acquired in a 7 point linear dither pattern, in which the binary was shifted up and down the detector in $4.5''$ steps. Ten exposures were acquired at each dither position. After culling the data for bad images, a total of 703 exposures at $2.123\ \mu\text{m}$ and 384 exposures at $1.648\ \mu\text{m}$ remained.

Calibration of the image data was carried out in the customary way. Flat field calibration was performed using twilight sky flats. Sky subtraction was performed by forming the median of the dithered exposures and subtracting this median from each exposure. Finally, $3.8''$ subimages centered on each of the two binary members were extracted from each exposure for use in the analysis below. The angular extent of these subimages was chosen to encompass all residual scattered light.

4. Data Analysis

A prediction of the PSF at the location of the binary companion was formulated for each exposure using the method described in Section 2. Each subimage of the guide star was Fourier transformed to form the guide star OTF. An anisoplanatic OTF was computed for each measured turbulence profile using the observing wavelength, aperture diameter, angular offset to the binary companion, and zenith angle at the time of the measurement. For each adaptive optics exposure, an anisoplanatic OTF was formed for the time of the exposure by interpolating the anisoplanatic OTFs computed for the nearest turbulence profile measurements. The pointwise product of the guide star OTF and the interpolated anisoplanatic OTF was formed, and the resulting OTF was Fourier transformed to generate a PSF prediction for the binary companion sampled at the 25 mas pixel scale of the PHARO image data.

For each exposure, the Strehl ratios of each observed binary member and of the predicted companion PSF were calculated. To compute these Strehl ratios, an ideal, diffraction limited PSF

for the Hale 5m was simulated by forming the pupil plane wavefront, Fourier transforming to form the image plane wavefront, and computing the square modulus. The pupil plane wavefront used in this procedure accounted for the shadows cast by the secondary mirror and the four struts that support it. For each subimage this diffraction limited PSF was normalized to have the same integrated signal, and the Strehl ratio was computed as the ratio of the peak value in the image to that of the ideal PSF. In these observations the $2.12 \mu\text{m}$ images were oversampled at 1.7 times Nyquist, while the $1.65 \mu\text{m}$ images were oversampled at 1.3 times Nyquist. This oversampling mitigates many of the subtle effects that can arise in computing Strehl ratios from image data (Roberts et al. 2004).

In addition to the Strehl ratio analysis, a direct comparison was carried out between the predicted and observed PSFs of the binary companion. Because the guide star PSF was used in formulating this prediction, the predicted PSF represents the image that would be obtained for a point source with the same brightness as the guide star. In fact the binary companion has a different brightness, which may be varying in time. Possible sources of such variability include the presence of cirrus clouds during observations or intrinsic photometric variability of the star itself. In addition, subimages were extracted from the PHARO exposures at a specific angular offset. Variations in the binary offset may occur from one exposure to the next, and it is of interest to measure these offsets from the data. These parameters constitute the differential photometry and astrometry of the binary, and their measurement requires a fit of the predicted companion PSF to the observed companion PSF.

For this analysis, a simple four parameter model was used. The relationship between an observation of the binary companion $P(x, y)$ and the predicted PSF $R(x, y)$ was taken to be

$$P(x, y) = bR(x - \Delta x, y - \Delta y) + c \quad (13)$$

Here b represents the differential amplitude between the two binary members, while Δx and Δy represent the differential angular offsets. The constant c models any differential in the background level of the guide star and companion data, and guarantees that the residuals from the fit have zero mean. Solution of this equation is readily performed using the predicted and observed companion OTFs. In OTF space, the parameters Δx and Δy induce a phase slope by the shift theorem (Bracewell 1986). A χ^2 merit function is readily formulated in this space, and minimization of this function leads to a simple iterative solution for all four parameters.

The outcome of this fitting procedure permits measurement of the differential astrometry and photometry between binary members. The overall angular offsets assumed in the subimage extraction were added to the fitted values of Δx and Δy to yield the differential astrometric offset between the binary members. The differential photometry was computed as the ratio of the total flux of the fitted PSF to that of the guide star. Because the residuals are zero mean, the total flux of the fitted PSF is identical to that of the observed image of the binary companion. At first glance, the use of the fitted PSF appears to provide no advantage over the observed PSF. However, these images were oversampled and their OTFs were lowpass filtered to suppress spatial frequencies

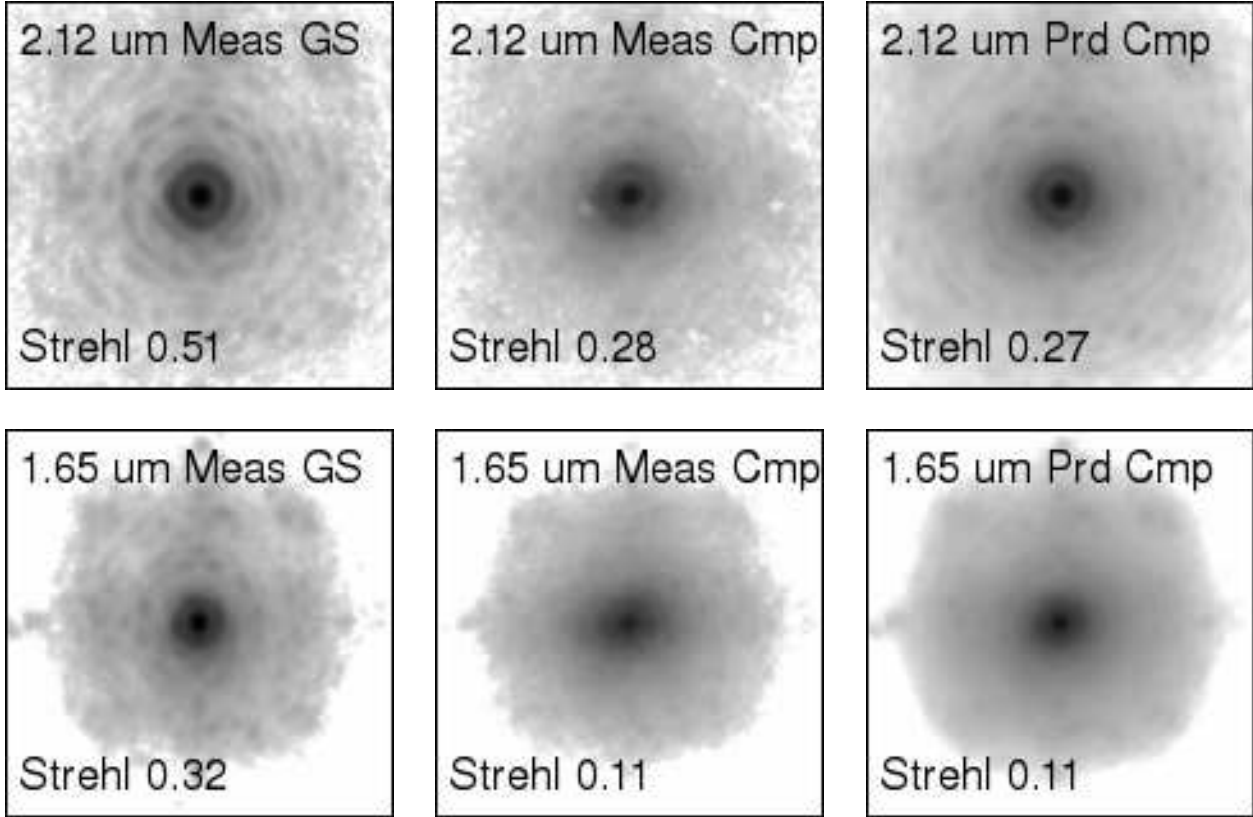


Fig. 4.— Observations of the guide star HD164984 and its companion HD164983 at $2.12 \mu\text{m}$ and $1.65 \mu\text{m}$. These observations were formed by integrating five sequential exposures, and are displayed on a log stretch. The angular offset between these stars is 21.3 arcsecs, and only a 2 arcsec field surrounding each star is shown. The first and second columns show observations of the guide star and companion, respectively. The predicted PSF of the companion appears in the third column, and was formulated from the product of the guide star OTF and the anisoplanatic OTF as described in Section 2. The Strehl ratios are shown at the bottom of each image. In these data, anisoplanatism has degraded the Strehl ratio of the companion by factors of two to three relative to the guide star. This degradation is accurately captured in the predicted companion PSF.

larger than the cutoff set by the telescope aperture. This filtering step substantially reduces the noise in the image.

5. Results

Examples of the $2.12 \mu\text{m}$ and $1.65 \mu\text{m}$ observations of the binary members are shown in Figure 4. These observations were integrated over five sequential exposures, and serve to illustrate the

quality of the AO compensation delivered by the PALAO system. In the particular 14 second observation at $2.12 \mu\text{m}$ shown in this figure, the guide star Strehl ratio was 51%. Due to the effects of anisoplanatism, the measured Strehl ratio of the binary companion was degraded to 28%. The predicted companion PSF computed from the guide star OTF and the turbulence profile at the time of this observation is also shown in this figure. The Strehl ratio calculated for the predicted companion PSF was 27%. The level of agreement between measured and predicted companion Strehl is a strong indication that the OTF model in Equation 5 accurately captures the effects of anisoplanatism. This also implies that the turbulence profiles measured by the DIMM/MASS equipment and used in this model reflect the true distribution of atmospheric turbulence. A similar level of agreement is seen for the 7 second observation at $1.65 \mu\text{m}$ shown in the same figure.

Figure 5 shows the values of r_0 and θ_0 computed from the measured turbulence profiles that were acquired over the course of the three hour observation. These parameters have been computed for the zenith angle of the guide star, which varied between 30 and 40 degrees during the observations. The values of these turbulence parameters display considerable temporal variation. Figure 5 also shows the time dependence of the Strehl ratios at $2.12 \mu\text{m}$. These Strehl ratios have again been averaged over five sequential exposures. The measured guide star Strehls vary significantly, and show little correlation with the Fried parameter. This suggests that sources of wavefront error other than residual fitting error contributed significantly to the guide star error budget. The measured Strehl ratios of the binary companion are also plotted, along with the Strehl ratios computed from the predicted companion OTF. As in Figure 4, these predictions are in excellent agreement with the measurements, and are able to track the companion Strehl ratio to a few percent despite a factor of two variability in the measured Strehl ratio of both the guide star and the companion. Also plotted are the Strehl ratios of the binary companion predicted using a traditional error budget approach. These predictions were generated from the product of the guide star Strehl ratio and the anisoplanatic Strehl ratio computed using the θ_0 approximation, as described in Section 2.3. These predictions fall well below the measurements, as expected from the discrepancies in the anisoplanatic Strehl ratio shown in Figure 2. Lastly, Figure 5 contains a plot of measured vs. predicted $2.12 \mu\text{m}$ and $1.65 \mu\text{m}$ Strehl ratios for the binary companion. This plot again illustrates strong agreement between the measured Strehl ratios and those derived using the predicted companion OTF.

Results from fitting the predicted companion PSF to the data are shown in Figure 6 for the observations shown in Figure 4. This figure shows that the prediction of the companion PSF slightly overestimates the core and underestimates the wings of the observed PSF. Horizontal cuts through the simulated diffraction limited PSF display complex morphology arising from light scattered by the four struts supporting the secondary mirror. The scattered light is most pronounced along the horizontal and vertical axes of the image, which are aligned with the support struts. Horizontal cuts through the residuals indicate that the predicted companion PSF agrees with the observations to about 10% accuracy at any point in the image. Stated another way, this PSF fitting procedure has improved the dynamic range of the observation by an order of magnitude.

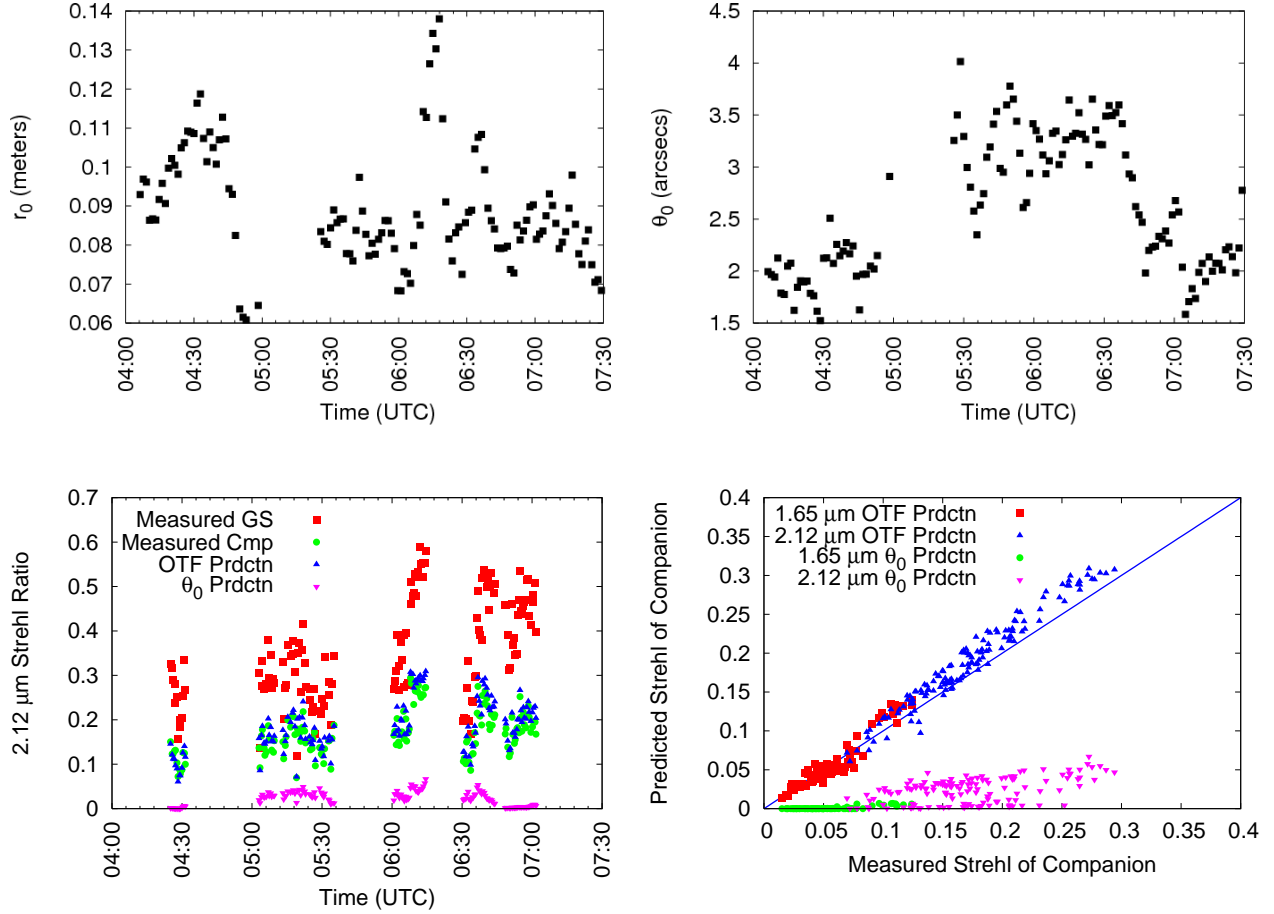


Fig. 5.— Turbulence parameters and Strehl ratios over the course of the observations. The upper panels show the Fried parameter and isoplanatic angle at $.5 \mu\text{m}$ computed for the zenith angle of the guide star, which ranged from 30 to 40 degrees over the three hour observation. The lower left panel shows the measured $2.12 \mu\text{m}$ Strehl ratios of the guide star and companion. Also plotted are the Strehl ratios predicted from the OTF formulation in Section 2, and predicted using the θ_0 approximation described in the text. The lower right panel shows the predicted vs. measured Strehl ratio of the binary companion. Strehl ratios at both $2.12 \mu\text{m}$ and $1.65 \mu\text{m}$ are included in this plot. These plots indicate that the OTF formulation accurately predicts the Strehl ratio degradation that arises from anisoplanatism. See the electronic edition of the Journal for a color version of this figure.

These residuals display two regimes, in which the accuracy of the predictions was limited by different effects. At radii less than about $.5 \text{ arcsecs}$, the residuals were dominated by systematic errors between the model and the observed data. These systematics may arise from a number of different effects. The power spectrum of atmospheric turbulence may be non-Komolgorov, so that Equation 12 is only approximately correct. Accuracy in the turbulence profile measurements from

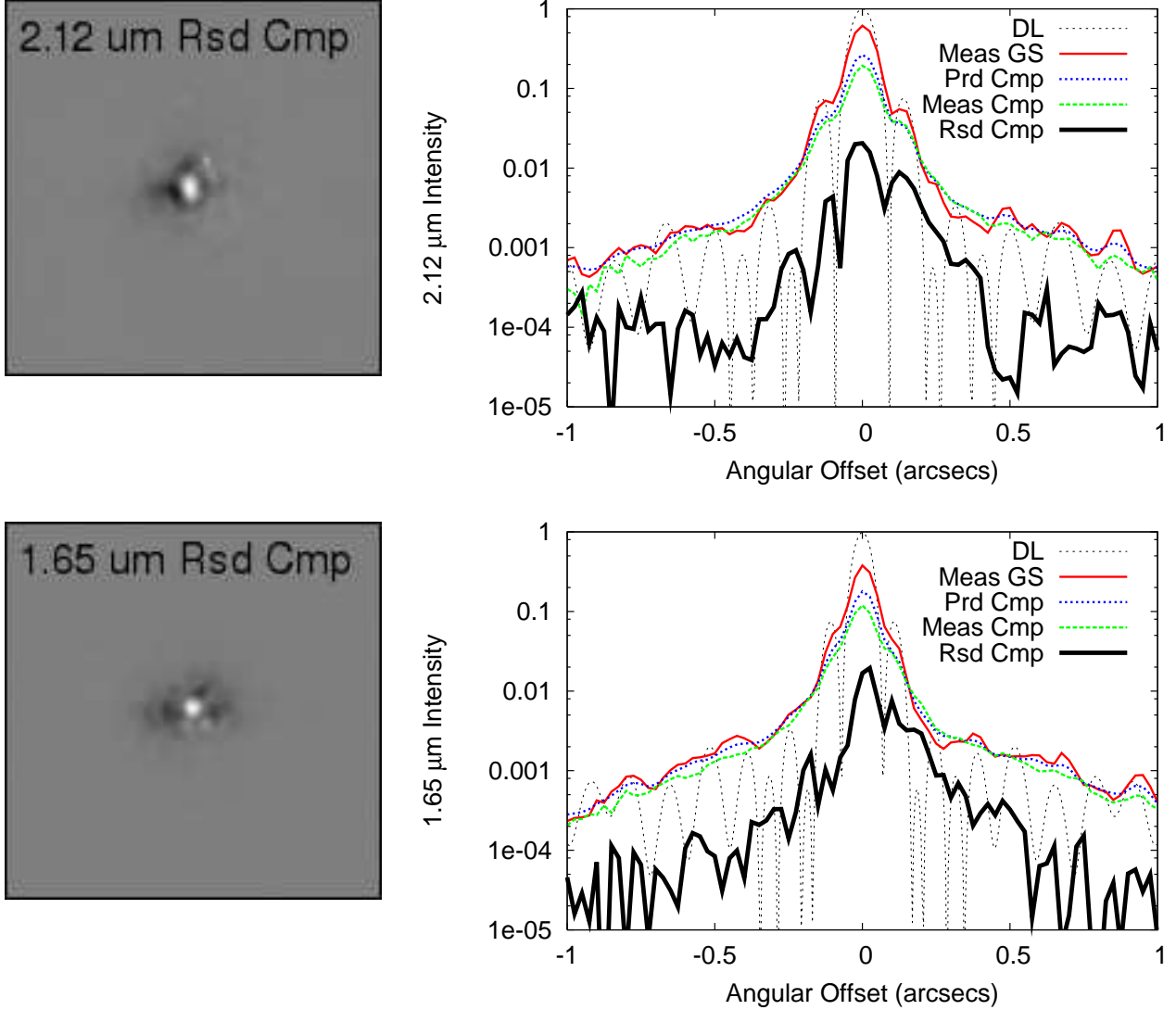


Fig. 6.— Results of fitting the model of the companion PSF to the observed data for the $2.12 \mu\text{m}$ and $1.65 \mu\text{m}$ observations shown in Figure 4. The left column shows the residuals in a 2 arcsec field around the companion, displayed on a log stretch. The right column shows horizontal cuts through the simulated diffraction limited PSF, the observed guide star PSF, and the predicted and observed companion PSF. The complex behavior displayed in the wings of the diffraction limited PSF arises from light scattered by the struts supporting the secondary mirror. The magnitude of the residual difference between the predicted and measured companion PSF is also plotted. At any point within the image, the predicted companion PSF matches the observed data to an accuracy of about 10 percent. See the electronic edition of the Journal for a color version of this figure.

the DIMM/MASS unit may limit the quality of the prediction. Finally, nonlinear response or charge diffusion in the infrared detector in PHARO may generate differential errors between the measured guide star and companion PSFs. At an angular separation of about .5 arcsecs, the signal level in the residuals dropped below a noise floor. This noise floor is set by a combination of the detector read noise, shot noise and quantization noise in the analog to digital conversion. The dominant source of noise depends on the efficacy of the lowpass spatial filtering that was performed on the OTF, which itself depends on the degree to which the images were oversampled. Further investigation will be required to determine the noise source that limits the precision of this technique in these two regimes.

At a radius of .5 arcsecs the value of the residual intensity was 3 to 4 orders of magnitude less than the peak of the measured companion. This level of PSF rejection is comparable to that achieved in near infrared AO observations that employ a Lyot coronograph. These systems provide about 4 to 5 orders of magnitude rejection at an offset of 1" from a star (Oppenheimer et al. 2000; Nakajima et al. 2005). In comparing Lyot coronography to this fitting technique, a disadvantage of the latter is that it requires the use of another star to serve as the PSF reference. On the other hand, Lyot coronographs employ an opaque focal plane mask that limits the inner working radius of the observation. For example, the Lyot coronograph in PHARO has masks with diameters of .41 and .91 arcsecs. There is no inner working radius in this fitting technique.

Figure 7 shows the differential photometry between the binary members derived from fitting the predicted companion PSF to the observed data. The timeseries of differential photometric measurements shows periods of substantial variability at 05:30 UT for the 2.12 μm observations, and at 07:15 UT for the 1.65 μm observations. The origin of this variability is not clear, but could plausibly be ascribed to cirrus. When these data were excluded, the standard deviation of the measured differential photometry was 1 part in 10^2 for both the 2.12 μm and 1.65 μm exposures. The mean differential photometry between the binary members is shown in column 2 of Table 1. The uncertainties quoted on these measurements are the estimated errors of the mean (Bevington & Robinson 1992), and are less than 1 part in 10^3 .

This level of photometric stability may be compared to recent results. Roberts et al. (2004) obtained differential photometric stability of order 1 part in 10^2 in J, H, and K band adaptive

Table 1. Differential photometry and astrometry for the binary system HD164984+HD164983.

λ (μm)	Differential Photometry	σ_{\parallel} (arcsec)	σ_{\perp} (arcsec)	ρ (arcsec)	P.A. (deg)
2.12	.7903 \pm .0004	.0152	.0100	21.3322 \pm .0006	282.3923 \pm .0011
1.65	.8316 \pm .0007	.0228	.0154	21.3306 \pm .0012	282.3932 \pm .0023

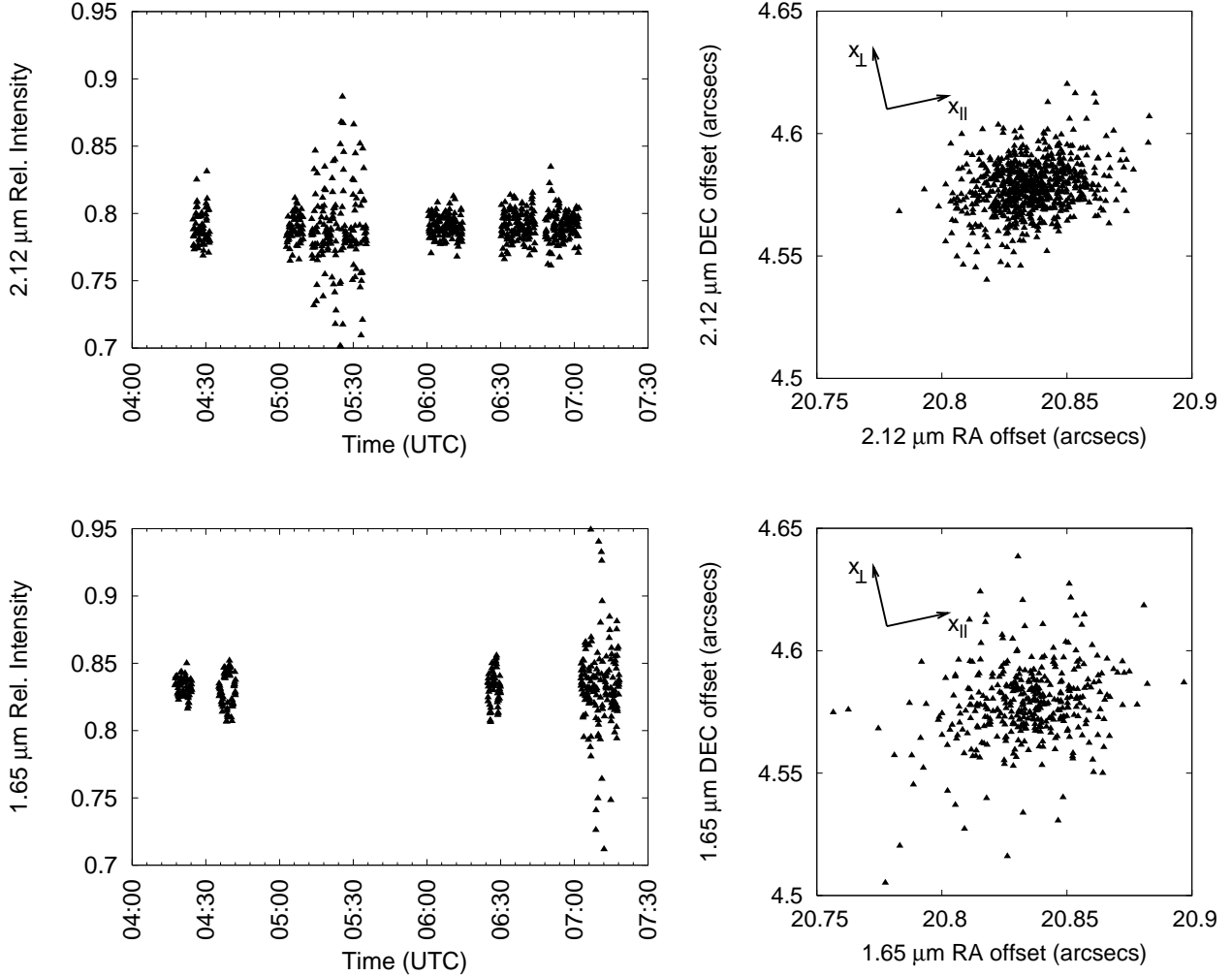


Fig. 7.— Differential photometric and astrometric measurements of the binary HD164984+HD164983 for 2.12 μm (upper) and 1.65 μm (lower) observations. Each point in these plots corresponds to a single 2.8 second exposure at 2.12 μm , or 1.4 second exposure at 1.65 μm . The left panels show the measured flux ratio of the companion to primary throughout the course of the observations. The right panels show the measured differential angular offset between the binary members for each exposure in the experiment. The elliptical scatter in the astrometric data arises from differential atmospheric tilt jitter between the two stars that is induced by atmospheric turbulence. This tilt jitter is predicted to be larger along the orientation of the binary, which lies along the x_{\parallel} axis indicated in these plots.

optics observations of several binary systems on the Advanced Electro-Optical System (AEOS) 3.6 m telescope. Seeing limited observations in the optical at the 6.5 m Multiple Mirror Telescope (MMT) (Hartman et al. 2005) and in the near infrared at the 3.8 m United Kingdom Infra-Red

Telescope (UKIRT) (Snellen 2005) displayed differential photometric stability of 1 part in 10^3 . All of these observations employed broader filters and lower total integration times than were used in this experiment. Relative to seeing limited observations, the sensitivity gains provided by adaptive optics have afforded this level of photometric stability at much lower flux levels, allowing observations of fainter targets. This technique may be usefully applied to observations of eclipsing binaries, transiting planets, and other systems that display photometric variability in the near infrared.

Figure 7 also shows the differential astrometry derived from the fit. Each exposure yielded a single measurement, all of which were combined to form the scatter plots in this figure. The astrometric offsets display an elliptical scatter, with larger errors along the axis connecting the binary members. This behavior is consistent with that of differential atmospheric tilt jitter, which arises from anisoplanatism of the tilt component of atmospheric turbulence. This effect leads to a random, achromatic fluctuation in the relative displacement of two objects. The standard deviation of this tilt jitter differs along the axes parallel and perpendicular to the orientation of the binary. A three term approximation to the parallel and perpendicular components of the variance arising from differential atmospheric tilt jitter is given by Sasiela (1994).

$$\begin{bmatrix} \sigma_{\parallel}^2 \\ \sigma_{\perp}^2 \end{bmatrix} = 2.67 \frac{\mu_2}{D^{1/3}} \left(\frac{\theta}{D} \right)^2 \begin{bmatrix} 3 \\ 1 \end{bmatrix} - 3.68 \frac{\mu_4}{D^{1/3}} \left(\frac{\theta}{D} \right)^4 \begin{bmatrix} 5 \\ 1 \end{bmatrix} + 2.35 \frac{\mu_{14/3}}{D^{1/3}} \left(\frac{\theta}{D} \right)^{14/3} \begin{bmatrix} 17/3 \\ 1 \end{bmatrix} \quad (14)$$

Here the turbulence moments μ_m are defined as

$$\mu_m = \int_0^\infty dz C_n^2(z) z^m \quad (15)$$

Using the mean turbulence profile over the three hour observation, the parallel and perpendicular components of differential atmospheric tilt jitter were computed from Equation 14 to be $\sigma_{\parallel} = 36$ mas and $\sigma_{\perp} = 21$ mas. These values are somewhat larger than those measured from the astrometric data, which appear in columns 3 and 4 of Table 1. The discrepancy likely arises from the finite integration time of the exposures. Assuming a characteristic wind speed of 5 m/s, these integration times are comparable to the wind crossing time for the 5 meter aperture, suggesting that tilt jitter has partially averaged away. This hypothesis is further supported by the reduction in tilt jitter between the 1.4 second exposures at $1.65 \mu\text{m}$ and the 2.8 second exposures at $2.12 \mu\text{m}$.

The mean differential astrometry between the binary members is shown in columns 5 and 6 of Table 1. A PHARO pixel scale of .02522 asec/pixel was used in the calculation (Metchev & Hillenbrand 2004). The uncertainties quoted for these measurements are again the estimated errors of the mean. This uncertainty is about 1 mas in the binary separation ρ , and a few arcsecs in position angle. Note that the differential astrometry of the $2.12 \mu\text{m}$ and $1.65 \mu\text{m}$ observations are in agreement at about the 1σ level. This provides an independent validation of the accuracy of these measurements.

This level of accuracy may be compared to recent astrometric results obtained with the adaptive optics system on AEOS. Roberts et al. (2004) performed I band adaptive optics observations of a

number of binaries and measured the differential astrometry to accuracies of 10 to 20 mas. These binaries had separations up to 5 arcsecs. Drummond et al. (2003) reported H band observations of a 400 mas binary with an astrometric precision of 1 mas. Note that to leading order the tilt variance in Equation 14 scales as $\theta^2/D^{7/3}$, so that these binaries suffer much less from differential atmospheric tilt jitter than the 21 arcsec binary observed in this experiment. Compared to the observations at Palomar reported here, both of these experiments employed broader filters and lower total integration times.

These results may also be compared to those obtained using other astrometric techniques. An astrometric accuracy of order 100 μ as has been achieved on the Palomar Testbed Interferometer (PTI) for a 30 arcsec binary (Lane et al. 2000), and recently accuracies of tens of μ as have been obtained for binaries with separations less than an arcsec (Lane & Muterspaugh 2004; Muterspaugh et al. 2006). This instrument has a limiting magnitude of about 6 due to the 40 cm size of its apertures. The STEPS program on the Hale 5m telescope at Palomar has achieved astrometric accuracies of less than 1 mas using seeing limited observations in the visible. (Pravdo & Shaklan 1996). These observations employed a 2 arcminute field of view and imaged crowded fields so as to establish an astrometric reference grid from the multiple objects in the field. Both of these techniques employ much broader filters than were used in the observations reported here. Further experiments will be required to understand the circumstances under which the astrometric technique described in Section 4 is competitive with these other methods. Generally speaking, the sensitivity improvements afforded by adaptive optics on a 5 meter aperture will permit application of this methodology to fainter limiting magnitudes than are accessible with PTI or STEPS, substantially increasing the number of accessible targets. Differential atmospheric tilt jitter scales as $D^{-7/6}$, and application of this technique on a larger aperture telescope will reduce this jitter while at the same time increasing the signal to noise ratio and decreasing the width of the PSF core. This would provide substantial improvements on the astrometric accuracies that have been reported in this experiment.

6. Conclusions

The research presented here has drawn together a number of different elements in order to generate predictions of the adaptive optics PSF. Factorization of the OTF in Equation 5 permits one to use the guide star PSF as a reference for observations throughout the field of view. This PSF encapsulates the complex behavior of the adaptive optics system that is otherwise very difficult to model. The covariance expression in Equation 6 provides an analytic formulation that captures the dependencies of anisoplanatism on aperture diameter, observing wavelength, turbulence profile, angular offset and zenith angle. Measurements of the turbulence profiles from the DIMM/MASS equipment provide the one input parameter for these predictions that is not determined directly from the observations. These three elements provide a methodology for adaptive optics PSF prediction that is accessible to direct experimental validation.

The binary star observations described above are in excellent agreement with these predictions. The Strehl ratios computed from the predicted companion PSFs match the measured values to an accuracy of a few percent, despite a factor of two temporal variability in both the guide star and companion Strehl ratios. The predicted companion PSF matches observations to about 10% out to radii of 1 arcsec. While this agreement serves to validate the predictive methodology, it must be emphasized that the adaptive optics PSF depends on a large number of parameters. This three hour experiment has tested these predictions over a very modest region of the underlying parameter space. A broader application of this methodology at shorter observing wavelengths, over wider fields of view, and under diverse turbulence conditions will provide a more stringent test. In some observing conditions these predictions will almost certainly fail due to the approximations discussed in Section 2. Likewise, the target of this experiment was a relatively bright binary whose members are of nearly identical magnitude. Additional observations will be required to understand the degree to which the photometric and astrometric precision and the contrast levels reported here are attainable in more diverse observational programs. Experiments at Palomar and Keck Observatories are currently being planned to perform this experiment on more binaries, and to employ this methodolgy on crowded field image data using both natural and laser guide star AO systems.

Agreement between the predicted and observed companion PSF indicate a level of consistency between turbulence profile measurements from the DIMM/MASS equipment and the effects of anisoplanatism on the AO compensated image quality. Both Multiaperture Scintillation Spectrometry and anisoplanatism are sensitive to higher altitude turbulence, but each is sensitive to the underlying turbulence statistics in a different way. The former is sensitive to aberrations introduced by short spatial wavelengths, which give rise to scintillation. In contrast, anisoplanatism arises from aberrations at all spatial wavelengths, though the manner in which these aberrations contribute depends on the altitude of the turbulence and the spatial frequency of the aberration. In this way, these two types of measurements are sampling different spatial frequency ranges of the turbulence power spectrum. At some level the consistency of the predictions and observations serve to validate the assumption of a Komolgorov turbulence spectrum. Further efforts will be required to understand the level of agreement implied by these and future results. One possible approach is to perform a sensitivity analysis by generalizing Equation 6 to include other classes of power spectra. An analysis of this type has been carried out by Lazorenko (2002), who considered the effects of non-Komolgorov power spectra on differential atmospheric tilt jitter.

These results suggest several lines of longer term development that may be of direct benefit to a number of astronomical applications. The plot of Strehl ratio vs. guide star offset shown in Figure 2 illustrates that the benefits of adaptive compensation occur over fields much larger than anticipated from the θ_0 approximation. This suggests that adaptive optics systems with fields of view of order several arcminutes may be usefully employed for near infrared observations. One of the challenges in interpreting these data over wide fields arises from the temporal and field dependent evolution of the adaptive optics PSF. The methodology described above allows a quantitative analysis of

such wide field observations that can account for these effects. The photometric and astrometric results presented in Section 5 and the dynamic range improvements implied by Figure 6 serve as illustrations of the astronomical potential of this methodology. Application of this technique to the imaging and deconvolution of crowded fields and extended objects would constitute a natural progression. The approach could readily be applied to the deconvolution of both image data and spatially resolved spectra acquired with an integral field unit.

Lastly, agreement between predictions and observations serve as an important on-sky validation that anisoplanatism is accurately understood in the context of near infrared astronomical observations over arcminute fields of view. Anisoplanatism constitutes the fundamental process underlying the use of tomography in adaptive optics. Tyler (1994) describes the application of the phase covariance in Equation 6 in combining wavefront measurements from multiple guide stars to form an estimate of the wavefront in a different direction. That this same expression has been used in this research to accurately predict the anisoplanatic degradation of the near infrared adaptive optics PSF over an arcminute field is a strong indication that tomographic algorithms will be successful in the same observational context.

The author would like to thank many colleagues who participated in discussions of this research, including Brent Ellerbroek, Richard Dekany, Mitchell Troy, Andrei Tokovinin, Keith Taylor, Andrew Pickles, Roger Smith, Don Gavel and Matthias Schoeck. The author gratefully acknowledges the efforts of the Thirty Meter Telescope site testing group and the Palomar Observatory staff in setting up and maintaining the turbulence monitoring equipment at Palomar Observatory.

This paper was prepared as part of the work of the Thirty Meter Telescope (TMT) Project. TMT is a partnership of the Association of Universities for Research in Astronomy (AURA), the Association of Canadian Universities for Research in Astronomy (ACURA), the California Institute of Technology, and the University of California. The partners gratefully acknowledge the support of the Gordon and Betty Moore Foundation, the U.S. National Science Foundation (NSF), the National Research Council of Canada, the Natural Sciences and Engineering Research Council of Canada, and the Gemini Partnership.

This work has also been supported by the National Science Foundation Science and Technology Center for Adaptive Optics, managed by the University of California at Santa Cruz under cooperative agreement No. AST - 9876783.

Facilities: Hale

A. Three Familiar Results in Adaptive Optics

This Appendix uses Equation 6 to recover three familiar results in adaptive optics. These results serve to illustrate the validity of Equation 6, and its broad applicability in performing

analytic and numerical calculations in adaptive optics. Equation 6 represents the piston removed phase covariance on a circular aperture in the presence of Komolgorov turbulence, and the three results below are valid under these assumptions.

A.1. Phase Structure Function for Uncompensated Turbulence

As a first example, consider the phase structure function $D_\phi(\vec{r}_1, \vec{r}_2)$ in the presence of uncompensated turbulence.

$$\begin{aligned} D_\phi(\vec{r}_1, \vec{r}_2) &= \langle [\phi(\vec{r}_1) - \phi(\vec{r}_2)]^2 \rangle \\ &= \langle [\phi(\vec{r}_1)]^2 \rangle + \langle [\phi(\vec{r}_2)]^2 \rangle - 2 \langle \phi(\vec{r}_1) \phi(\vec{r}_2) \rangle \end{aligned} \quad (\text{A1})$$

The three covariance functions may be rewritten in terms of Equation 6. In the resulting expression, all dependencies on the functions G_1 and G_2 drop out in the difference, leaving only

$$D_\phi(\vec{r}_1, \vec{r}_2) = 2^{8/3} \Xi k^2 |(\vec{r}_1 - \vec{r}_2)|^{5/3} \int dz C_n^2(z) \quad (\text{A2})$$

Define the Fried parameter r_0 as

$$r_0^{-5/3} = 2^{8/3} \frac{\Xi}{\Lambda} k^2 \int_0^\infty dz C_n^2(z) \quad (\text{A3})$$

where the constant Λ is

$$\Lambda = 2 \left[\frac{24}{5} \Gamma \left(\frac{6}{5} \right) \right]^{5/6} = 6.88388 \quad (\text{A4})$$

The phase structure function may be rewritten in terms of r_0 as

$$D_\phi(\vec{r}_1, \vec{r}_2) = \Lambda \left(\frac{|\vec{r}_1 - \vec{r}_2|}{r_0} \right)^{5/3} \quad (\text{A5})$$

This is the well known expression for the piston removed phase structure function on a circular aperture in the presence of Komolgorov turbulence.

A.2. Aperture Averaged Phase Variance for Uncompensated Turbulence

As a second example, the aperture averaged phase variance in the presence of uncompensated turbulence is evaluated. This quantity may be computed by integrating the phase variance $\langle [\phi(\vec{r})]^2 \rangle$ over the circular aperture and dividing by the area of the aperture. The phase variance may be rewritten using Equation 6, yielding

$$\frac{4}{\pi D^2} \int d\vec{r} \langle [\phi(\vec{r})]^2 \rangle = \frac{\Lambda}{2^{8/3}} \left(\frac{D}{r_0} \right)^{5/3} \left\{ \left[\frac{8}{\pi D^2} \int d\vec{r} G_1 \left(\left| \frac{2}{D} \vec{r} \right| \right) \right] - G_2(0) \right\} \quad (\text{A6})$$

The integral over the hypergeometric function in G_1 may be performed term by term, yielding

$$\begin{aligned} \frac{8}{\pi D^2} \int d\vec{r} G_1 \left(\left| \frac{2}{D} \vec{r} \right| \right) &= \frac{12}{11} {}_2F_1 \left(-\frac{11}{6}, -\frac{5}{6}; 2; 1 \right) \\ &= \frac{12}{11} \frac{\Gamma(2)\Gamma(\frac{14}{3})}{\Gamma(\frac{23}{6})\Gamma(\frac{17}{6})} \end{aligned} \quad (\text{A7})$$

where the second equality has employed the relationship (Abramowitz & Stegun 1972)

$${}_2F_1(a, b; c; 1) = \frac{\Gamma(c)\Gamma(c-a-b)}{\Gamma(c-a)\Gamma(c-b)} \quad (\text{A8})$$

The second term in Equation A6 may be written

$$\begin{aligned} G_2(0) &= \frac{2^{11/3}}{\pi} \int_0^1 dy y^{8/3} \left[\cos^{-1} y - y \sqrt{1-y^2} \right] \\ &= \frac{9}{187} \frac{2^{28/3}}{\pi} \frac{\left[\Gamma(\frac{7}{3}) \right]^2}{\Gamma(\frac{14}{3})} \end{aligned} \quad (\text{A9})$$

The integral has been evaluated analytically using the substitution $y = \cos \psi$. Further manipulations involving relationships between Gamma functions or direct numerical calculation show that the first term evaluates to exactly twice the second. The resulting expression becomes

$$\begin{aligned} \frac{4}{\pi D^2} \int d\vec{r} \left\langle [\phi(\vec{r})]^2 \right\rangle &= \frac{6}{11} \frac{\Gamma(2)\Gamma(\frac{14}{3})}{\Gamma(\frac{23}{6})\Gamma(\frac{17}{6})} \frac{\Lambda}{2^{8/3}} \left(\frac{D}{r_0} \right)^{5/3} \\ &= 1.03242 \left(\frac{D}{r_0} \right)^{5/3} \end{aligned} \quad (\text{A10})$$

This is the well known result for the aperture averaged phase variance in the presence of uncompensated turbulence.

A.3. Aperture Averaged Residual Phase Variance from Anisoplanatism

As a final example of particular relevance to this paper, consider the aperture averaged residual phase variance due to anisoplanatism. This quantity may be computed by integrating the residual phase variance $\left\langle [\phi_b(\vec{r}) - \phi_a(\vec{r})]^2 \right\rangle$ over the circular aperture and dividing by the area of the aperture. Again using Equation 6, we find

$$\begin{aligned} \frac{4}{\pi D^2} \int d\vec{r} \left\langle [\phi_b(\vec{r}) - \phi_a(\vec{r})]^2 \right\rangle &= \frac{4}{\pi D^2} \int d\vec{r} \left[\left\langle (\phi_b(\vec{r}))^2 \right\rangle + \left\langle (\phi_a(\vec{r}))^2 \right\rangle - \right. \\ &\quad \left. 2 \left\langle \phi_a(\vec{r}) \phi_b(\vec{r}) \right\rangle \right] \\ &= 2\Xi k^2 D^{5/3} \int_0^\infty dz C_n^2(z) \left\{ \left| \vec{\Omega}_{ab}(z) \right|^{5/3} + \right. \end{aligned} \quad (\text{A11})$$

$$\begin{aligned}
& G_2 \left(\left| \vec{\Omega}_{ab}(z) \right| \right) - G_2(0) + \\
& \frac{4}{\pi D^2} \int d\vec{r} \left[G_1 \left(\left| \frac{2}{D} \vec{r} \right| \right) - G_1 \left(\left| \frac{2}{D} \vec{r} + \vec{\Omega}_{ab}(z) \right| \right) + \right. \\
& \left. G_1 \left(\left| \frac{2}{D} \vec{r} \right| \right) - G_1 \left(\left| \frac{2}{D} \vec{r} - \vec{\Omega}_{ab}(z) \right| \right) \right] \}
\end{aligned}$$

The first term is

$$\begin{aligned}
2\Xi k^2 D^{5/3} \int_0^\infty dz C_n^2(z) \left| \vec{\Omega}_{ab}(z) \right|^{5/3} &= 2^{8/3} \Xi k^2 \left| \vec{\theta}_{ab} \right|^{5/3} \int_0^\infty dz C_n^2(z) z^{5/3} \quad (\text{A12}) \\
&= \left(\frac{\left| \vec{\theta}_{ab} \right|}{\theta_0} \right)^{5/3}
\end{aligned}$$

where the isoplanatic angle θ_0 is defined as

$$\theta_0^{-5/3} = 2^{8/3} \Xi k^2 \int_0^\infty dz C_n^2(z) z^{5/3} \quad (\text{A13})$$

This is the well known isoplanatic angle approximation to the aperture averaged residual phase variance due to anisoplanatism.

Consider expanding the remaining three pairs of terms in Equation A11 in a Taylor series about $\vec{\Omega}_{ab}(z) = 0$. The constant terms cancel in the differences. The linear term in $\vec{\Omega}_{ab}(z)$ vanishes in the function $G_2 \left(\left| \vec{\Omega}_{ab}(z) \right| \right)$, since it is a function only of the magnitude of this vector. The linear term in $\vec{\Omega}_{ab}(z)$ also vanishes in the sum of the terms $G_1 \left(\left| 2\vec{r}/D - \vec{\Omega}_{ab}(z) \right| \right)$ and $G_1 \left(\left| 2\vec{r}/D + \vec{\Omega}_{ab}(z) \right| \right)$, since this vector enters these two terms with opposite sign. Thus, the remaining terms in Equation A11 have a leading order dependence of $\left| \vec{\Omega}_{ab}(z) \right|^2$. These terms are only slightly higher order than the first term in this equation, and their contribution to the aperture averaged residual phase variance can be significant even at modest angular offsets. This is illustrated by the large discrepancy between the isoplanatic angle approximation to the aperture averaged residual phase variance and the exact result shown in Figure 2.

REFERENCES

Abramowitz, M., & Stegun, I. A., Handbook of Mathematical Functions, New York: Dover, 1972

Beckers, J. M. 1988, Very Large Telescopes and their Instrumentation, ESO Conference and Workshop Proceedings, Proceedings of a ESO Conference on Very Large Telescopes and their Instrumentation, Garching: European Southern Observatory (ESO), 1988, ed. Marie-Helene Ulrich., p.693, 693

Bevington, P. R., & Robinson, D. K. Data Reduction and Error Analysis for the Physical Sciences, New York: McGraw-Hill, 1992

Bracewell, R. N., *The Fourier Transform and Its Applications*, New York: McGraw-Hill, 1986

Christou, J. C., Pugliese, G., Köhler, R., & Drummond, J. D. 2004, PASP, 116, 734

Diolaiti, E., Bendinelli, O., Bonaccini, D., Close, L., Currie, D., & Parmeggiani, G. 2000, A&AS, 147, 335

Drummond, J., Milster, S., Ryan, P., & Roberts, L. C. 2003, ApJ, 585, 1007

Ellerbroek, B., Britton, M., Dekany, R., Gavel, D., Herriot, G., Macintosh, B., & Stoesz, J. 2005, Proc. SPIE, 5903, 20

Flicker, R. & Rigaut, F. 2005, J. Opt. Soc. Am. A 22, 504

Fusco, T., Conan, J.-M., Mugnier, L. M., Michau, V., & Rousset, G. 2000, A&AS, 142, 149

Goodman, J. W., *Statistical Optics*, New York: Wiley, 1985

Hammer, F., et al. 2004, Proc. SPIE, 5382, 727

Hartman, J. D., Stanek, K. Z., Gaudi, B. S., Holman, M. J., & McLeod, B. A. 2005, AJ, 130, 2241

Hayward, T. L., Brandl, B., Pirger, B., Blacken, C., Gull, G. E., Schoenwald, J., & Houck, J. R. 2001, PASP, 113, 105.

Kornilov, V., Tokovinin, A. A., Vozyakova, O., Zaitsev, A., Shatsky, N., Potanin, S. F., & Sarazin, M. S. 2003, Proc. SPIE, 4839, 837

Lane, B. F., Colavita, M. M., Boden, A. F., & Lawson, P. R. 2000, Proc. SPIE, 4006, 452

Lane, B. F., & Mutterspaugh, M. W. 2004, ApJ, 601, 1129

Lazorenko, P. F. 2002, A&A, 382, 1125

Léna, P., & Lai, O. 1999, *Adaptive Optics in Astronomy*, 351

Metchev, S. A., & Hillenbrand, L. A. 2004, ApJ, 617, 1330

Mutterspaugh, M. W., Lane, B. F., Konacki, M., Burke, B. F., Colavita, M. M., Kulkarni, S. R., & Shao, M. 2006, A&A, 446, 723

Nakajima, T., et al. 2005, Astronomische Nachrichten, 326, 952

Oppenheimer, B. R., Dekany, R., Hayward, T., Brandl, B., & Troy, M. 2000, IAU Symposium, 202,

de Pater, I., Marchis, F., Macintosh, B. A., Roe, H. G., Le Mignant, D., Graham, J. R., & Davies, A. G. 2004, Icarus, 169, 250

Pravdo, S. H., & Shaklan, S. B. 1996, ApJ, 465, 264

Roberts, L. C., et al. 2004, Proc. SPIE, 5490, 504

Sasiela, R. J., Electromagnetic Wave Propagation in Turbulence, Berlin: Springer, 1994

Skidmore, W., et al. 2004, Proc. SPIE, 5489, 154

Snellen, I. A. G. 2005, MNRAS, 363, 211

Steinbring, E., et al. 2002, PASP, 114, 1267

Tokovinin, A., Baumont, S., & Vasquez, J. 2003, MNRAS, 340, 52

Tokovinin, A., Vernin, J., Ziad, A., & Chun, M. 2005, PASP, 117, 395

Troy, M., et al. 2000, Proc. SPIE, 4007, 31

Tyler, G. 1983, J. Opt. Soc. Am. A 1, 251

Tyler, G. 1994, J. Opt. Soc. Am. A 11, 409

Veran, J., Rigaut, F., Matre, H. & Rouan, D. 1997, J. Opt. Soc. Am. A 14, 3057

Vernin, J., & Munoz-Tunon, C. 1995, PASP, 107, 265

Voitsekhovich, V. V., Orlov, V. G., Cuevas, S., & Avila, R. 1998, A&AS, 133, 427

Weiβ, A., Hippler, S., Kasper, M., Woorder, N., & Quartel, J. 2002, ASP Conf. Ser. 266: Astronomical Site Evaluation in the Visible and Radio Range, 266, 86